www.sciencemag.org/content/359/6380/1131/suppl/DC1

Supplementary Materials for

Coherent, atomically thin transition-metal dichalcogenide superlattices with engineered strain

Saien Xie, Lijie Tu,* Yimo Han,* Lujie Huang, Kibum Kang, Ka Un Lao, Preeti Poddar, Chibeom Park, David A. Muller, Robert A. DiStasio Jr., Jiwoong Park†

*These authors contributed equally to this work.
†Corresponding author. Email: jwpark@uchicago.edu

Published 9 March 2018, *Science* **359**, 1131 (2018)
DOI: 10.1126/science.aao5360

This PDF file includes:

Materials and Methods
Supplementary Text
Figs. S1 to S13
Table S1
References

Materials and Methods

Modulated MOCVD growth of monolayer TMD superlattices

The synthesis of monolayer TMD superlattices was performed in a 2-inch quartz tube furnace (Fig. S1A). Tungsten hexacarbonyl (THC), molybdenum hexacarbonyl (MHC), diethyl sulfide (DES), and dimethyl selenide (DMSe) were selected as chemical precursors for W, Mo, S and Se, respectively. THC and MHC were kept in bubblers at a constant pressure of 800 Torr and introduced into the furnace with Ar as the carrier gas at room temperature. All precursors were introduced into the growth furnace with individual mass flow controllers (MFCs) regulating their flow rates. The growth of the superlattices was kept at a constant temperature of 600 ^oC and a total pressure of 2 Torr throughout. Flow rates of all precursors were kept constant during the growth except for the chalcogens: 20 sccm of THC or MHC with Ar as the carrier gas, 1 sccm H_2 and 350 sccm Ar, 0.3 sccm DES, and 0.4 sccm DMSe. The flow of the chalcogen precursors was alternated with breaks (typically 2 min) in between for purging purposes (see schematic in Fig. S1B). The growth time of different superlattices is summarized in Table S1, and relative width of the superlattices ($\rho = d_{WS2}/d_{WSe2}$) is proportional to the relative growth time (t_{WS2}/t_{WSe2}), as shown Fig. S1D. The stable growth environment is crucial for coherent superlattice growth. In contrast, the synthesis with a temperature decrease (3 min, down to 300 ^oC) between different TMD growths result in heterostructures without lattice coherence. These heterostructures show incoherent diffraction patterns (Fig. 2E and Fig. S3 right), no PL tuning (Fig. S10 left), and no out-of-plane rippling (Fig. S12D). After the superlattice growth process, the furnace was naturally cooled down to room temperature in an inert environment with a constant flow of Ar. NaCl was placed at the upstream region of the furnace. The main growth substrate used was 285 nm SiO_2/Si. For more discussion of our MOCVD process, see ref. 22.

TEM analysis

Sample preparation: The monolayer TMD superlattice was spin-coated with PMMA A4, and then the substrate was etched in KOH 1M solution. After being rinsed in deionized water for three times, the PMMA supported superlattice was transferred to a TEM grid with 10 nm thick SiN windows, and the chip was annealed in an ultra-high vacuum (10^{-7} Torr) at 350 ºC for 3 hours to remove the PMMA.

SAED and DF-TEM: SAED patterns were taken using an FEI Tecnai T12 Spirit, operated at 80 kV. The selective area aperture has a diameter of 280 nm. The dark-field TEM images are taken by selecting specific diffraction spots (*39*).

ADF-STEM: ADF-STEM imaging was performed using a FEI TITAN operated at 120 kV with a ~15 pA probe current. A 30 mrad convergence angle and a ~40 mrad inner collection angle were used for all ADF-STEM images, whose contrast is proportional to Z^{γ}, where Z is the atomic number and $1.3 < \gamma < 2$.

EMPAD: Lattice spacing and rotation maps were performed using an electron microscope pixel array detector (EMPAD) (25), which is a high-speed, high dynamic range diffraction camera with the sensitivity to measure a diffraction pattern from a single atom (*40*). We used a 120-kV electron beam with a 0.5 mrad convergence angle to record diffraction patterns at every point in 2D real space scan to build up a 4-dimensional phase space map. By measuring the center of the second order diffraction spots using center of mass calculation, we mapped reciprocal lattice vectors for every scan position in real space. The inverse of these vectors provided the real-space lattice spacing maps shown in Fig. 2F (the lattice spacing in the armchair direction was multiplied by √3 to get the normalized $a_{//}$, therefore makes the unstrained hexagonal lattice have same $a_{//}$ and $a_{\perp}$). The rotation map in Fig. 2G was calculated by measuring the rotation angles of

the reciprocal lattice vectors as a function of real-space scan positions. The color scale was normalized to the mean value of the entire sample region. (1 for the lattice constant map and 0 for the rotation map).

Photoluminescence measurements

The PL spectra were acquired using Horiba Lab RAM HR Evolution confocal Raman microscope, with a 532-nm laser excitation under ambient conditions. The PL images were taken with a widefield PL microscope using band pass filters with 10 nm bandwidth, and the center photon energies of 1.75 eV, 1.82 eV, 1.91 eV, and 2.00 eV, respectively (*41*).

Device fabrication, electrical transport and electroluminescence measurements

All devices were fabricated with as-grown heterostructures on 285 nm SiO_2/Si growth substrates. We first defined the source and drain electrodes using standard e-beam lithography, followed by e-beam evaporation of 0.5 nm Ti/50 nm Au. After lifting off using acetone, we defined the device channel and etched the unwanted TMD regions with SF_6 and O_2 plasma etching. All electrical measurements were performed under ambient conditions using a custom-built probe station with a Keysight B1500A Semiconductor Device Analyzer. EL measurements were carried out using the widefield PL microscope used for PL measurement.

Supplementary Text

Device applications of WS_2/WSe_2 heterostructures

Our 2D superlattices have dislocation-free heterointerfaces with precisely controlled nanoscale supercell dimensions. These two advanced properties are crucial for producing practical devices that are difficult to produce otherwise. To demonstrate this, we have fabricated and examined three types of devices based on our coherent heterostructures—*p-n* diodes, LEDs, and double heterostructure (DH) transistors, where the coherent heterointerfaces were generated between WS_2 (*n*-type, in general) and WSe_2 (*p*-type).

High-performance p-n diodes: We have successfully fabricated electrical devices that include only one WSe_2-WS_2 (*p-n*) heterojunction between two metal electrodes (Fig. S8A, inset; see supplementary materials for fabrication methods). A representative p-n diode shows high forward-bias current (>10 μA) and low reverse-bias current (~10 pA), producing a high rectification ratio (>10^6), as illustrated in Fig. S8A. The high performance for our *p-n* diodes is consistent with the dislocation-free coherent heterointerfaces, as the coherent interfaces could minimize the scattering of carriers by dislocations, resulting in a higher electrical conductivity under forward bias. Furthermore, the defect-assisted hopping transport of charge carriers will be minimized, which accounts for a lower conductivity under reverse bias.

Electroluminescence in p-n diodes (LEDs): We further observed strong electroluminescence (EL) from the *p-n* diodes. The false-color EL image overlaid on the optical micrograph of the *p-n* heterostructure device confirms that the luminescence originates from the heterointerface between WS_2 and WSe_2 (Fig. S8B, interface marked with the dashed line). The EL is observed under the forward-bias condition, and its intensity dramatically increases with the injected current (*I*). For example, the EL from the device in Fig. S8C increases by three orders of

magnitude when I increases only by a factor of 5 (inset, Fig. S8C). The EL spectrum shows a peak similar to the PL peak from WS_2, which suggests that the light emission is likely to originate from the *e-h* recombination within WS_2. These observed features for EL and the back gate dependence (Fig. S8D) matches very well with the expected band alignment (Fig. S8D inset). The EL spectra at more positive gate bias (-30V) show multiple peaks suggesting that electrons (injected from WS_2 side) and holes (injected from WSe_2 side) recombine near the WS_2-WSe_2 heterointerface. However, it produces only a single peak from WS_2 under a more positive gate bias (-60V) as the hole carrier density increases in our device and dominates the current flow across the junction (into WS_2).

The high current needed for EL and the efficient radiative recombination both require the absence of dislocations. Therefore, the observation of EL suggests that the coherent heterointerface is crucial for high-performance LEDs. We note that all our devices are directly fabricated on the SiO_2/Si growth substrate without any encapsulation and the EL measurements were performed under ambient conditions. This suggests that its performance (brightness and stability) may be further improved, which calls for more comprehensive EL studies in the future to fully understand and optimize the optoelectronic properties of our coherent heterostructures.

Double heterostructure (DH) transistors: We successfully fabricated 2D double heterostructure devices, based on double coherent heterojunctions (WSe_2-WS_2-WSe_2) with the width of middle part (d_{ws2}) very narrow and precisely controlled. The schematic and band diagram are depicted in Fig. S9A, together with an SEM image of a representative DH device with $d_{WS2} \approx 90$ nm. Our DH devices (over 10 of such devices were studied) show symmetric, nonlinear *I-V* characteristics with no rectification behavior (Fig. S9B), as expected from their symmetric configuration. Their *p*-type transport is consistent with the band diagram shown in Fig. S9A, where the hole is the

main carrier and WS_2 region acts as a barrier. As these DH devices are conceptually similar to double-diodes connected in opposite directions, they may conduct only when the middle region is narrow with the device conductivity strongly dependent on d_{WS2}. This is indeed what we observe from our devices. (Fig S9C) The device with $d_{WS2} \approx 70$nm is approximately one order of magnitude more conductive than the device with $d_{WS2} \approx 90$nm, and we were unable to observe conduction for devices with d_{ws2} larger than 130 nm. This is also consistent with the depletion width of ~ 320 nm for TMD lateral heterostructures reported (*16*). Our demonstration of double heterostructures provides an example for building devices with designed band structures with excellent dimension control, which would stimulate further exploration of complex device applications.

Effective negative Poisson's effect in omnidirectional coherent epitaxy

Below, we explain the symmetry and lattice isotropy in the superlattice grown by omnidirectional coherent epitaxy, using a symmetry analysis. We use a square lattice to illustrate the symmetry constraint for simplicity. Conventional unidirectional coherent epitaxy only requires matched $a_{//}$ while $a_{\perp}$ is free of any constraints, thus $a_{\perp}$ of small (large) lattice becomes even smaller (larger), corresponding to $\delta_{\perp} > \Delta$ for positive Poisson's ratio (Fig. S6A). Therefore, the resulting heterostructure shows a different symmetry (rectangular) than that of the original crystal (square). However, in omnidirectional coherent epitaxy, the epilayers grown in all directions connect to each other without dislocation. As a result, the final heterostructure maintains the same symmetry with that of the original crystal, showing $\delta_{\perp} = 0$ (Fig. S6B). Similar results for our WS_2/WSe_2 superlattices is illustrated in Fig. 2I. The isotropic lattice

constants result in an effectively negative Poisson's effect, regardless of the intrinsic Poisson's ratios of each component, and is universal for any coherent omnidirectional epitaxy system.

Coarse-grained simulations of the TMD superlattice

To study the equilibrium state of the entire coherent TMD superlattice shown in Fig. 2, we developed and employed a coarse-grained force-field model that accounts for nearest-neighbor bonding and angular interactions. In this approach, the atom types are "dressed W atoms" and can either be [WS_2] or [WSe_2] units centered at the corresponding W atomic position in the 2D superlattice (depicted as red or blue circles, respectively, in Fig. S7A and S7B). The total potential energy expression employed for the superlattice is $E_{latt} = \frac{1}{2}\sum_{bonds} k_b(r - r_0)^2 + \frac{1}{2}\sum_{angles} k_\theta(\theta - \theta_0)^2$, in which the first term represents a harmonic bond potential (with k_b and r_0 representing the bond force constant and equilibrium bond distance, respectively) and the second term a harmonic angular potential (with k_θ and θ_0 representing the angular force constant and equilibrium angle, respectively). Figs. S7A and S7B summarize the different types of bond and angle terms encountered in our energy expression for TMD superlattices.

In all of our simulations, the central (seed) triangle consists of [WS_2] atom types (with a side length of 20 dressed atoms). The superlattice is then constructed *via* the addition of alternating TMD bands, the next of which is 4 (or 8) layers of [WSe_2] atom types, followed by 5 (or 10) layers of [WS_2] atom types, etc. until the model superlattice consists of 14 total TMD bands (for direct comparison with the experimental superlattice considered in Fig. 2). In this initial configuration, all bond lengths were set to a value of r = 3.22 Å, which is the mean of the experimental W—W distances in pure WS_2 (r_0 = 3.15 Å) and WSe_2 (r_0 = 3.29 Å) monolayers. For a given replica of the system (with a minimum of 6 replicas is always used) each of the

initial positions of the dressed atoms are randomized (up to 5% of the initial bond distance) before E_{latt} is minimized using second-order damped dynamics (with a damping parameter of $\gamma = 0.2$ and fictitious time step of $\delta t = 0.004$, which have been optimized to ensure rapid convergence to the energetic minimum).

To parameterize the bond terms, we utilized the 2D Young's moduli for pure WS_2 ($Y_{2D} = 140$ N/m) and WSe_2 ($Y_{2D} = 116$ N/m) monolayers obtained from highly accurate density functional theory calculations (*42, 43*) to set k_b= 1.2 Å^{-2} for [WS_2]—[WS_2] and k_b= 1.0 Å^{-2} for [WSe_2]—[WSe_2]. For dressed atoms at the interface (in which [WSe_2]—[WS_2] or [WS_2]—[WSe_2]), the appropriate k_b and r_0 are chosen to satisfy the outward growth mechanism of the TMD superlattice (see Fig. S7B for a graphical depiction).

Angular interactions were included to reflect the shear stiffness inside the TMD superlattice. In this regard, the larger the shear modulus is, the stronger is the tendency of the superlattice to maintain an equilateral triangular structure. Since the differential shear moduli for these TMD monolayers are unknown, we have studied a series of k_θ ranging from 0 rad^{-2} (0 deg^{-2}, no angular interactions) to 40 rad^{-2} (0.012 deg^{-2}, very strong angular interactions) with $\theta_0 = \pi/3$ rad $= 60^\circ$ in all cases. Quite importantly, we find that the inclusion of angular interactions is key to predicting the spatial patterns and histograms of both the parallel ($a_{//}$) and perpendicular ($a_\perp$) lattice constants (see Fig. S7C). With an intermediate-range value of k_θ= 20 rad^{-2} (0.006 deg^{-2}), we find excellent agreement with the experimental results for $a_{//}$ and $a_\perp$, as shown in Figs. 2F, 2H, and 2J.

Energetics governing the flat-rippled configuration space in strained WSe_2 monolayers

The model used to explore the energetics of the flat-rippled configuration space in a strained WSe_2 monolayer grown on an α-SiO_2 substrate was assembled using the QuantumWise nanoscience simulation software package (see Fig. S11A) (*44*). For consistency with the dimensions of the ripples observed from our TMD superlattices (see Fig. 4), we chose to model a WSe_2 monolayer ripple with a wavelength of $\lambda \approx 30$ nm and a width of $d_{WSe2} \approx 10$ nm (corresponding to the x- and y-axes, respectively, in Fig. S11A).

For the initial flat WSe_2 monolayer configuration, we started with an equilibrium WSe_2 monolayer consisting of 3,456 WSe_2 units with dimensions of x = 31.51 nm and y = 10.23 nm. Applying an isotropic axial strain of 4% in the x-direction (representing the lattice mismatch of $\Delta \approx 4\%$ between WSe_2 and WS_2 monolayers) coupled with transversal expansion in the y-direction (governed by Poisson's ratio of $\nu = 0.19$ for a WSe_2 monolayer (*42, 43*)), we arrived at our initial flat (and compressively strained) WSe_2 monolayer configuration with dimensions of x = 30.25 nm and y = 10.31 nm. We then proceeded to assemble the underlying α-SiO_2 substrate (with an interlayer separation of $R = 3.5$ Å, reflecting a typical separation distance between van der Waals (vdW) heterostructures (5)) consisting of 42,336 SiO_2 units with dimensions of x = 30.27 nm and y = 10.32 nm (chosen to minimize the periodic mismatch between the WSe_2 monolayer and the substrate). In the z-direction, we utilized 6 SiO_2 layers to account for the bulk properties of the SiO_2 substrate. As a result, our model for exploring the flat-rippled configuration space in this system contains a total of 137,376 atoms (with 10,368 atoms in the WSe_2 monolayer and 127,008 atoms in the α-SiO_2 substrate).

To introduce a ripple in the WSe_2 monolayer with height A (see Figs. 4B and S11A), we considered the series of (trough-to-trough) shapes formed by the sinusoidal family of functions

($\sin^n(x)$ with n = 2, 4, 8). In particular, these ripples were created by inducing a vertical displacement (*i.e.*, a z-coordinate change) in each atom contained in the WSe_2 monolayer based on its corresponding horizontal position (or x-coordinate) as follows:

(*i*) $z = A\sin^2\left(\frac{\pi x}{\lambda}\right) = \frac{A}{2} + \frac{A}{2}\sin(\frac{2\pi x}{\lambda} - \frac{\pi}{2})$.

(*ii*) $z = A\sin^4\left(\frac{\pi x}{\lambda}\right) = \mathrm{A}\sin^2(\frac{\pi x}{\lambda}) - \frac{A}{4}\sin^2(\frac{2\pi x}{\lambda})$.

(*iii*) $z = A\sin^8\left(\frac{\pi x}{\lambda}\right) = \mathrm{A}\sin^4(\frac{\pi x}{\lambda}) - \frac{A}{2}\sin^2(\frac{\pi x}{\lambda})\sin^2(\frac{2\pi x}{\lambda}) + \frac{A}{16}\sin^4(\frac{2\pi x}{\lambda})$.

These sinusoidal transformations govern the shape (or profile) of the ripple and are more compactly represented by S_1, S_2, and S_4, respectively, throughout the text.

Elastic energy for the WSe_2 monolayer: The elastic energy (E_{el}) for the WSe_2 monolayer as a function of the ripple height, A, for ripple shapes generated using the sinusoidal transformations (defined above) was computed using continuum mechanics as a sum of the stretching (E_s) and bending (E_b) energy components (defined below), each of which is depicted in Fig. S11B.

In this work, we adopted a harmonic potential energy expression (*i.e.*, Hooke's Law) to describe E_s as follows: $E_s = \frac{1}{2}Y_{2D}d_{WSe2}\frac{(L-L_0)^2}{L_0}$, in which Y_{2D} is the 2D Young's modulus (or 2D elastic stiffness) for a WSe_2 monolayer and $dL \equiv L - L_0$ is the amount by which the monolayer is stretched (or compressed) relative to the relaxed equilibrium length, L_0. Since the WSe_2 monolayer is comprised of only 3 atomistic layers, E_s for this system is more appropriately described by Y_{2D} instead of the 3D Young's modulus (Y_{3D}) as was found for other TMD systems such as MoS_2 as well as truly 2D materials such as graphene (*45, 46*). Throughout this work, we utilize the value of Y_{2D} = 116 N/m, which was obtained from highly accurate density functional theory calculations (*42, 43*).

For E_b we employed the following energy expression based on Euler buckling theory (*47, 48*): $E_b = \frac{1}{2} B d_{WSe2} \int dx z''(x)^2$, in which B is the bending stiffness and $z''(x)$ is the second derivative of the ripple shape with respect to x (the stretching/compression direction). We note here that significant controversy still exists in the literature regarding the use of classical shell/plate theory for B in 2D materials (such as TMD monolayers) as this approach suffers from the large uncertainty necessarily present in any definition of "thickness" in such ultra-thin nanofilms (*45*, *49–51*). Throughout this work, we completely sidestep this issue by utilizing a recent experimentally derived value of B = 12.4 eV (corresponding to WSe_2 with zigzag chirality (*52*)) and therefore avoid the use of any measure of "thickness" in our energy expressions.

Since the initial flat WSe_2 monolayer has been compressed by 4% (corresponding to the lattice mismatch with WS_2), this configuration starts with a relatively large $E_s \approx 50$ meV per WSe_2 while $E_b = 0$ meV (see Fig. S11B). As the ripple forms and A increases, L increases towards L_0 releasing the compression strain and steadily decreasing E_s; although this is accompanied by a simultaneous monotonic increase in E_b, the total $E_{el} = E_s + E_b$ is still dominated by E_s over the entire range of A before the energetic minimum for all ripple shapes considered herein. The location of the minimum in E_{el} is therefore primarily dictated by the minimum in E_s, although E_b can play a more substantive role and therefore shift the minimum to lower A values for ripple shapes induced by higher-order (and therefore more perturbative) sinusoidal transformations. For A values beyond the minimum, both E_s and E_b steadily increase as L is now larger than L_0 (corresponding to a stretched monolayer) and the degree of bending is becoming increasingly more severe.

Interlayer van der Waals (vdW) energy: To complete our description of the energetics governing the flat-rippled configuration space, we also account for the non-bonded and long-range vdW

interactions between the WSe_2 monolayer and the underlying SiO_2 substrate. Here we utilized two all-atom quantum mechanical vdW corrections (both the so-called D3 method (*53, 54*) with modified Becke-Johnson (BJ) damping (*55*) and a renormalized version of the "atoms-in-solids" variant (*56, 57*) of the Tkatchenko-Scheffler (TS-vdW) method (*58*) with Tang-Toennies (TT) damping (*59*)). In the D3 approach, the chemical environment (*via* the corresponding coordination number) of each atom has been accounted for in both the pairwise two-body (2B) vdW interactions, $E_{vdW-2B} = -\frac{1}{2}\sum_{AB}\sum_{n=6,8} s_n \frac{C_n^{AB}}{r_{AB}^n} f_{d,n}^{BJ}(r_{AB})$, and the beyond-pairwise three-body (3B) vdW interactions, $E_{vdW-3B} = \frac{1}{6}\sum_{ABC} \frac{C_9^{ABC}(3cos\theta_a cos\theta_b cos\theta_c+1)}{(r_{AB}r_{BC}r_{CA})^3} f_{d,3}^{BJ}(r_{ABC})$, *via* the isotropic *n*-th order dispersion coefficients ($C_6^{AB}, C_8^{AB}, C_9^{ABC}$). In these expressions, r_{AB} is the distance between atoms A and B, $\theta_a, \theta_b, \theta_c$ are the interior angles formed by the ABC triangle, and the scaling factors were set to s_6 = 1.0 and s_8 = 0.3589 throughout. To more accurately and reliably describe the vdW interactions in such complex nanostructures, we also utilized a renormalized version of the "atoms-in-solids" variant of TS-vdW, in which the electrodynamic screening from the environment of each atom has been accounted for via the Clausius-Mossotti equation and the corresponding experimental bulk dielectric functions (*60*), the Thomas–Reiche–Kuhn sum rule has been satisfied by all frequency-dependent atomic polarizabilities, and both 2B vdW interactions, $E_{vdW-2B} = -\frac{1}{2}\sum_{AB} \frac{C_6'^{AB}}{r_{AB}^6} f_{d,6}^{TT}(r_{AB})$, and 3B vdW interactions, $E_{vdW-3B} = \frac{1}{6}\sum_{ABC} \frac{C_9'^{ABC}(3cos\theta_a cos\theta_b cos\theta_c+1)}{(r_{AB}r_{BC}r_{CA})^3} f_{d,3}^{TT}(r_{ABC})$, were included with TT damping *via* the isotropic *n*-th order dispersion coefficients ($C_6'^{AB}$ and $C_9'^{ABC}$).

All vdW calculations were performed using an in-house program that accounts for periodic boundary conditions (in the x- and y-directions) in both the atomic coordination number determination as well as the 2B and 3B interlayer vdW energy computations. Further

modifications of the program were required to correctly deal with the different intrinsic periodicities of the WSe_2 monolayer and SiO_2 substrate.

In the initial flat WSe_2 monolayer, the interlayer vdW binding energy is largest (most negative) as the monolayer in this configuration is in closest contact with the underlying substrate (see Fig. S11B). As the ripple forms and A increases, the magnitudes of both the attractive $E_{vdW\text{-}2B}$ and repulsive $E_{vdW\text{-}3B}$ terms decrease, becoming less attractive and less repulsive, respectively. Since $|E_{vdW\text{-}3B}|$ is only about 1/3 of $|E_{vdW\text{-}2B}|$ (see Fig. S11B), their sum $E_{vdW} = E_{vdW-2B} + E_{vdW-3B}$ still remains attractive, although it becomes less attractive with increasing A. As expected, the overall decay rate (as a function of A) in the interlayer vdW binding energy decreases for ripple shapes generated with increasingly more perturbative (higher-order) sinusoidal transformations, reflecting the fact that more of the TMD monolayer is in close contact with the substrate in such ripple profiles.

Total energy analysis: The combination of E_{el} and E_{vdW} provides our total energy expression ($E_{tot} = E_{el} + E_{vdW}$), which is plotted as a function of A for the aforementioned sinusoidal ripple shapes in Fig. S11B (wherein E_{tot} was computed with respect to the flat monolayer configuration). Since the energetic contributions from E_{el} and E_{vdW} in this system are competitive in nature and similar in magnitude, their combination predicts a distinct energetic barrier separating the initial flat (and highly strained) configuration with the minimum-energy rippled configurations emerging in the range of $A = 2 - 4$ nm. Here we find that the rippled configurations with higher-order sinusoidal shapes are most stable, with a relative energy range that can be tuned with respect to the flat configuration. In this regard, the values of A predicted by these simple hybrid macroscopic-microscopic theoretical models are in relatively good agreement with the corresponding experimental measurements (see Fig. 4D). Quite interestingly, the renormalized "atoms-in-

solids" variant of TS-vdW, which is a more complete model for treating vdW interactions in such complex nanostructures, predicts that the buckled configurations are more stable than the strained flat configuration for all buckle shapes considered herein. This eliminates the need for more aggressive bending in the ML and is also accompanied by more accessible energetic barriers separating the rippled and flat states, both findings of which are completely consistent with our experimental observations.

Estimation of critical thickness

The critical thickness of WS_2/WS_2 epitaxial system based on People-Bean model (*35*) is given by

$$h_c \cong \frac{1-\nu}{1+\nu}\frac{1}{16\pi\sqrt{2}}\frac{b^2}{a}\frac{1}{\Delta^2}\ln[\frac{h_c}{b}]$$

Where a = 0.329 nm is the lattice constant of WSe_2. b is the length of Burgers vector, and we take b = a = 0.329 nm as it corresponds to the easiest formed misfit dislocation; ν is the Poisson's ratio of WSe_2. The numerical result of the above equation is plotted in Fig. S13, showing a critical thickness of 17 nm (ν = -0.2), 9.8 nm (ν = 0), and 5.4 nm (ν = 0.2) for WS_2/WSe_2 epitaxy system with Δ = 4%. We note that the People-Bean model is known to overestimate the critical thickness for Δ < 6.2% (*61*).

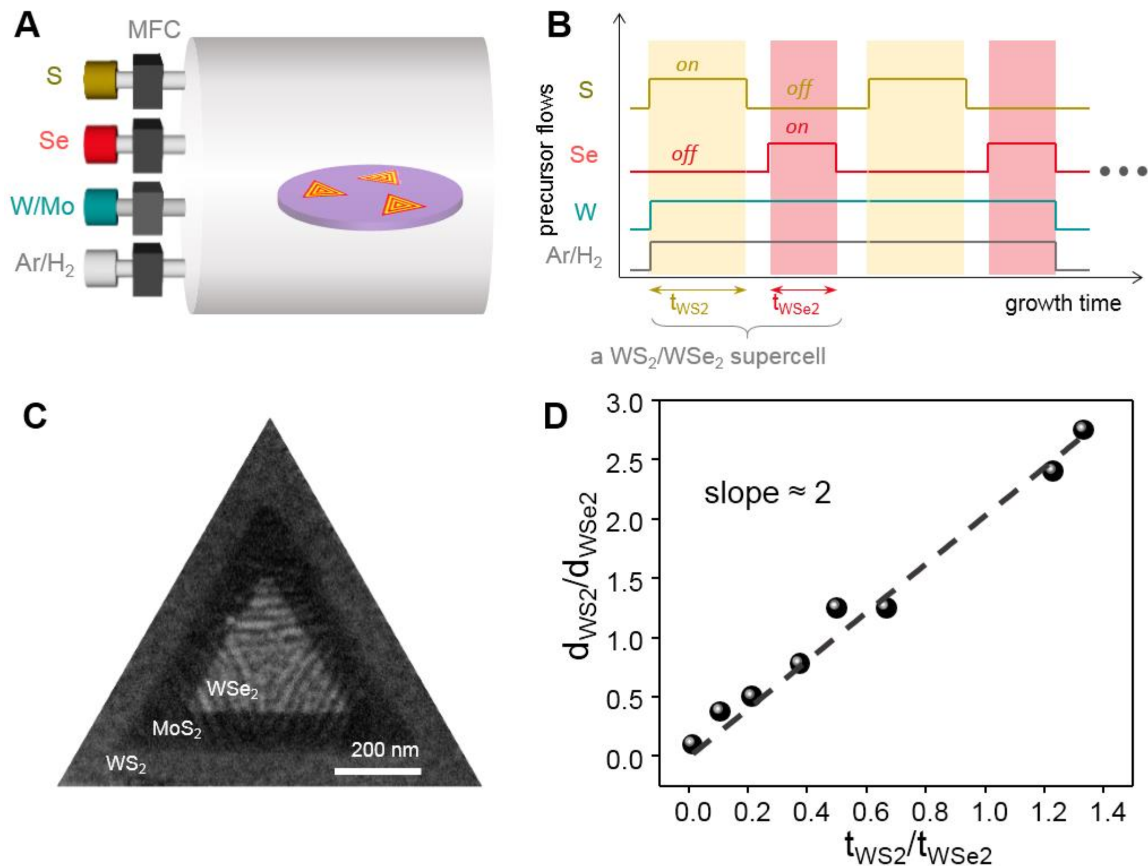

Fig. S1. Modulated-MOCVD process. (**A**) Schematic of modulated-MOCVD reactor with individual MFCs that precisely control the flow of all precursors. (**B**) Time sequence of the modulated superlattice growth where the growth time for a supercell {WS_2 and WSe_2} is {t_{WS2} and t_{WSe2}}. (**C**) SEM image of a coherent $WSe_2/MoS_2/WS_2$ heterostructure. (**D**) Plot of relative widths ($\rho = d_{WS2}/d_{WSe2}$) of superlattices versus relative growth time (t_{WS2}/t_{WSe2}) showing a linear dependence (Data of growth time for different superlattices summarized in Table S1).

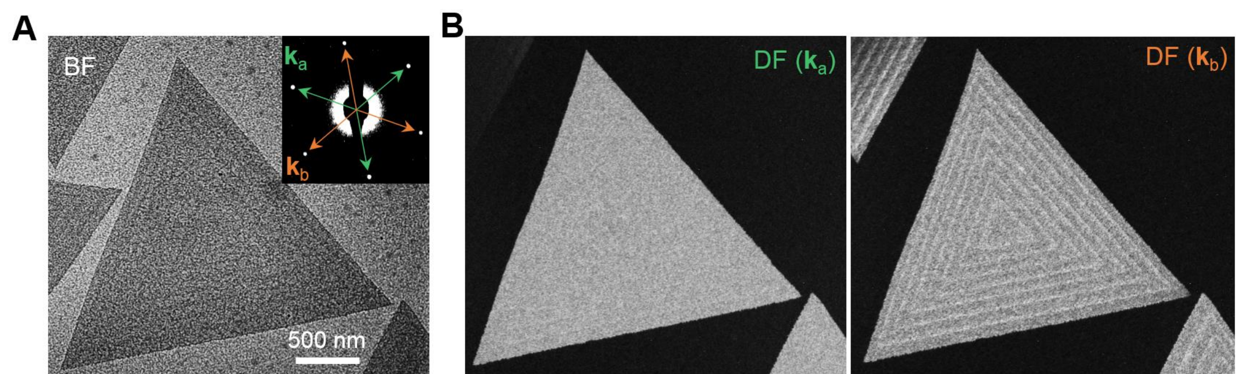

Fig. S2. TEM images of a WS_2/WSe_2 superlattice. (**A**) Bright-field image of superlattice {50 nm and 40 nm}. Inset: diffraction patterns with the first order spots divided into two families of $\mathbf{k}_a$ and $\mathbf{k}_b$. Scale bar, 500 nm. (**B**) Dark-field TEM images acquired by collecting from $\mathbf{k}_a$ and $\mathbf{k}_b$, respectively. The uniform contrast shown in DF ($\mathbf{k}_a$) suggests that $\mathbf{k}_a$ points towards the W-zigzag direction (*39*).

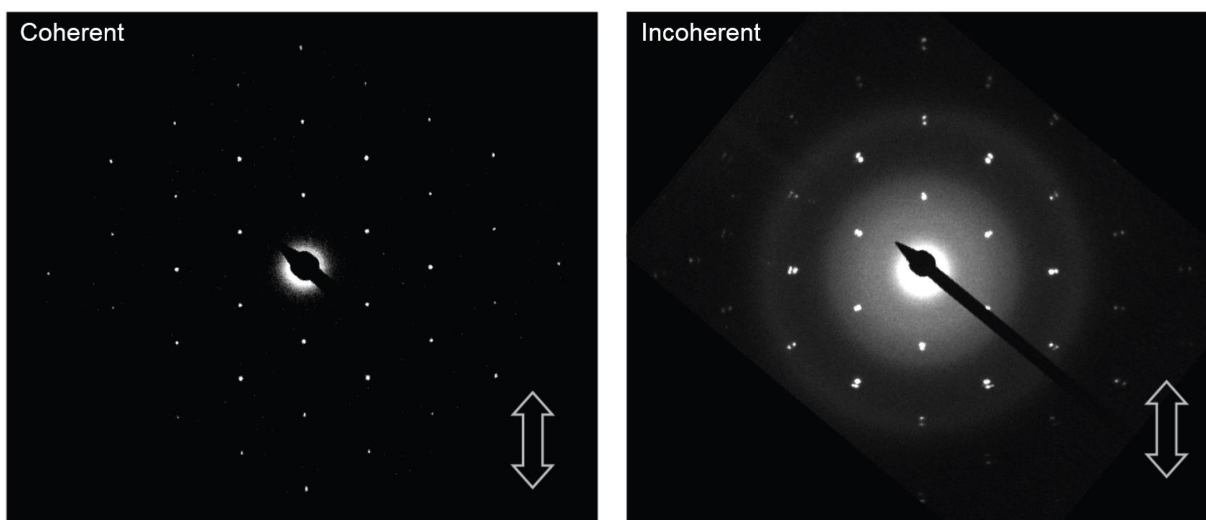

Fig. S3. SAED patterns of WS_2/WSe_2 heterostructures. Left, enlarged SAED pattern shown in Fig. 2C. Right, the full SAED pattern of an incoherent heterostructure from which Fig. 2E is taken.

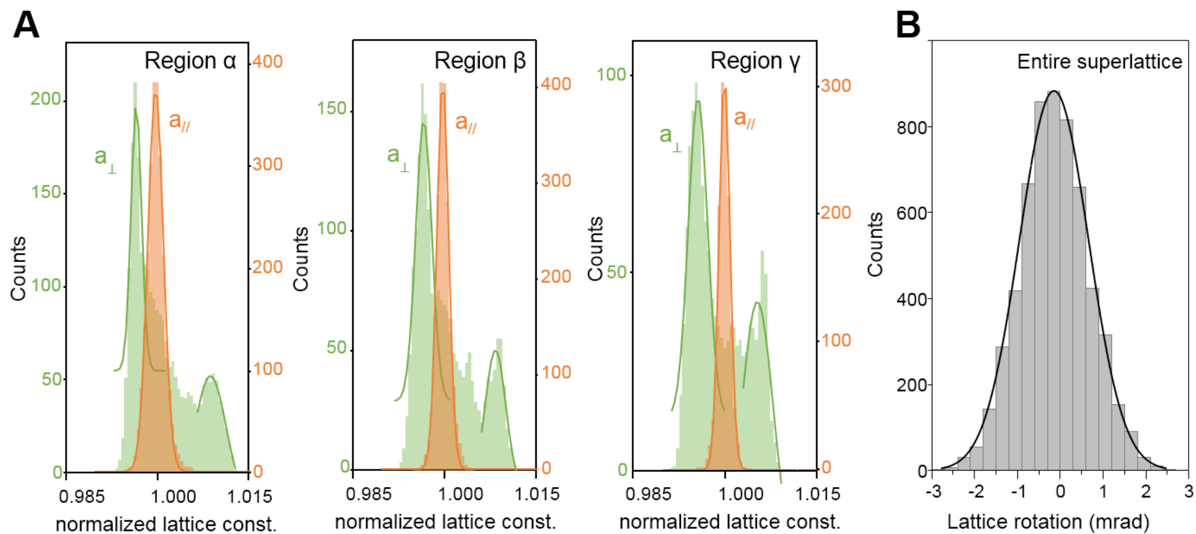

Fig. S4. Histograms of lattice parameters. (**A**) Histograms of $a_{//}$ and $a_{\perp}$ for region α (two $a_{\perp}$ peaks centered at 0.996 and 1.008), β (two $a_{\perp}$ peaks centered at 0.996 and 1.008), and γ (two $a_{\perp}$ peaks centered at 0.996 and 1.005). (**C**) Histogram of lattice rotation of the entire superlattice showing a standard deviation of 0.8 mrad.

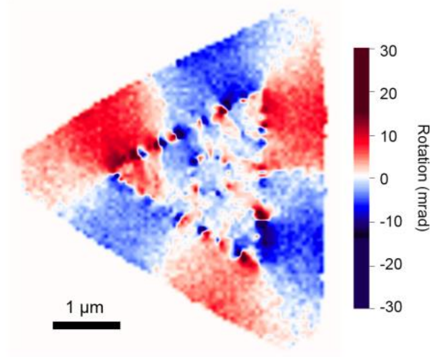

Fig. S5. Lattice rotation map of an incoherent WS_2/WSe_2 heterostructure. An incoherent WS_2/WSe_2 heterostructure showing arrays of dislocations at the heterointerfaces. Scale bar, 1 μm.

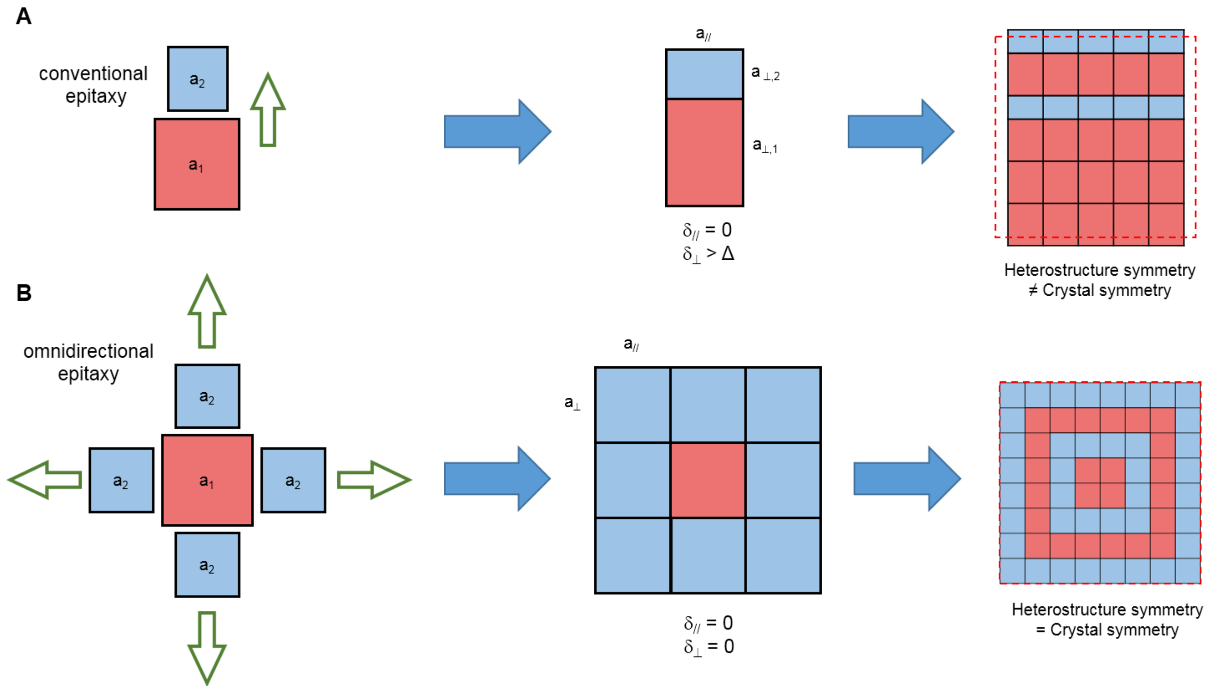

Fig. S6. Schematic of conventional and omnidirectional epitaxy. (**A**) Schematic of conventional unidirectional epitaxy and the resulting heterostructure with different symmetry from that of the original crystal. (**B**) Schematic of omnidirectional coherent epitaxy and the resulting heterostructure maintaining the same symmetry of the original crystal.

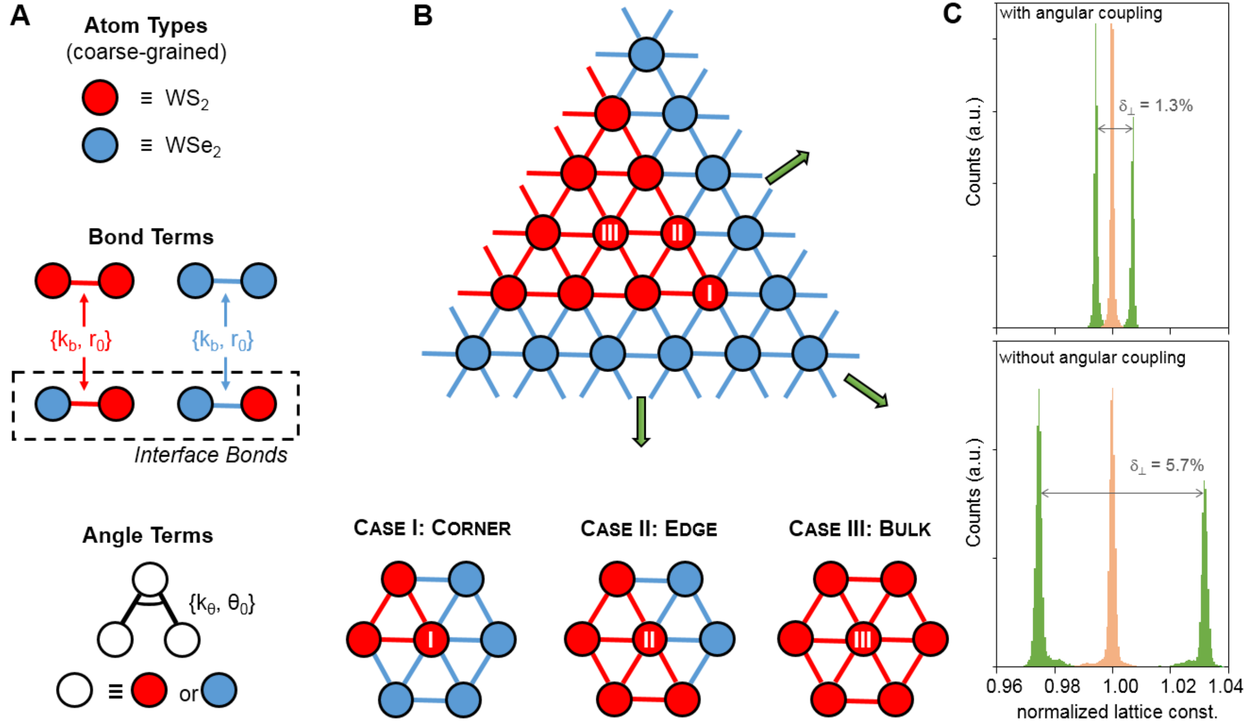

Fig. S7. Coarse-grained simulation of the WS_2/WSe_2 coherent superlattice. (**A**) Red and blue circles depict the atom types in this system: "dressed W atoms" that can either be [WS_2] or [WSe_2] units. There are four types of bond terms, depending on the dressed atom types and the interface conditions: [WS_2]—[WS_2], [WSe_2]—[WSe_2], [WS_2]—[WSe_2] (growth from [WS_2] to [WSe_2]) and [WSe_2]—[WS_2] (growth from [WSe_2] to [WS_2]). For the angular interactions, each of the three dressed atoms that form the angle can either be [WS_2] or [WSe_2]. (**B**) Three different environments for dressed atoms on an interior corner of the WS_2/WSe_2 superlattice. Green arrows denote the growth direction in the TMD superlattice. (**C**) Theoretical simulation results for the $a_{//}$ and $a_{\perp}$ distributions. The addition of angular coupling terms significantly reduces $\delta_{\perp}$ from 5.7 % to 1.3 %, in excellent agreement with the experimental observation of coherent epitaxy in both the parallel and perpendicular directions.

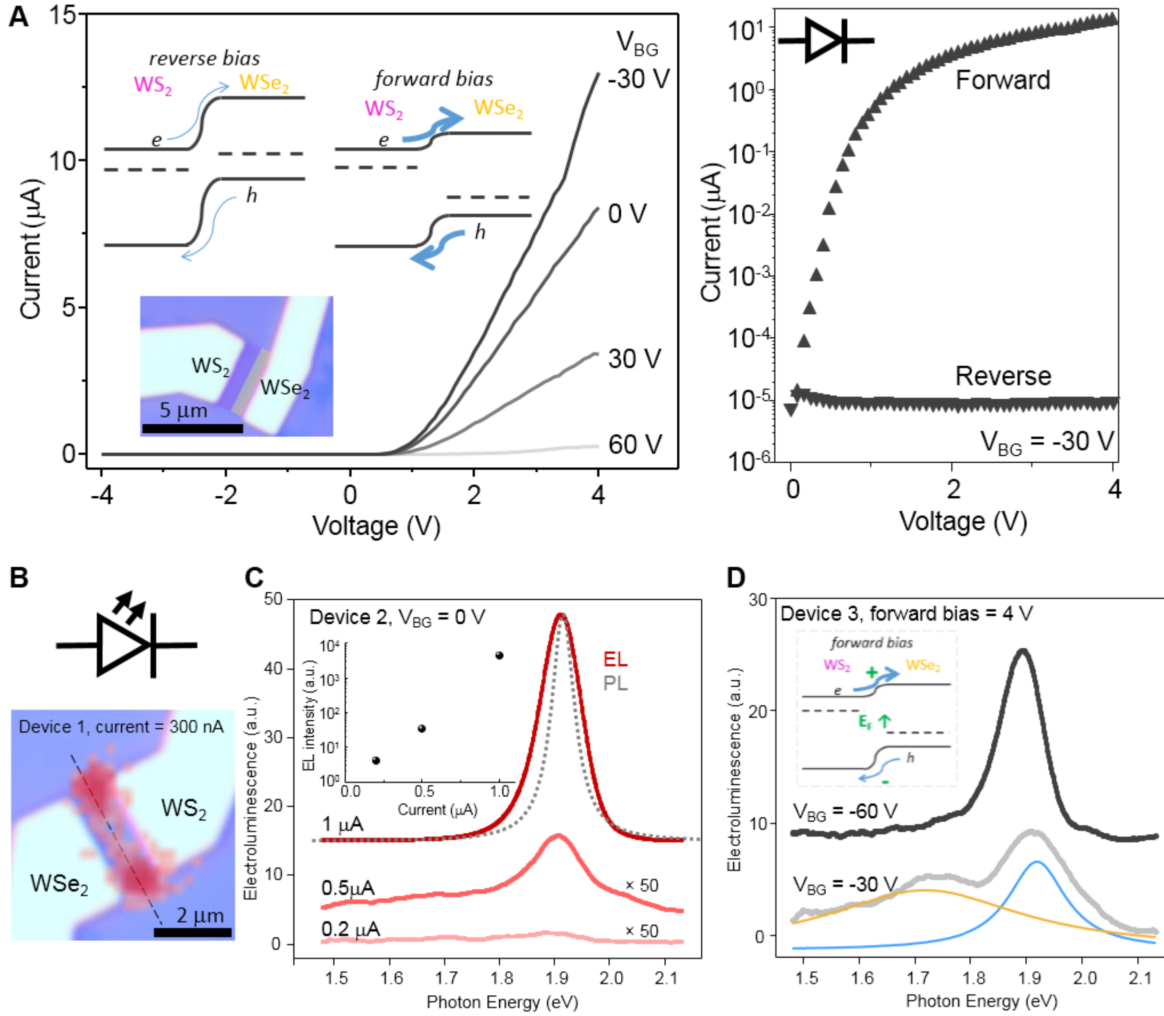

Fig. S8. Electrical transport and electroluminescence of WSe_2/WS_2 *p-n* diodes. (**A**) Current-Voltage (*I-V*) curves for a WSe_2-WS_2 p-n diode under different V_{BG} showing a rectification ratio of 10^6. (**B**) EL intensity (red) map overlaid with optical micrograph of the p-n diode device, showing the EL centered at WS_2-WSe_2 heterointerface (marked with dashed line). (**C**) EL spectra (red) under current $I = 0.2$, 0.5, and 1 μA, respectively, together with PL spectrum (grey). Inset: EL intensity for corresponding current intensity, showing an exponential dependence. (**C**) EL spectra recorded under V_{BG} = -60 and -30 V, with fitted peaks (blue and orange) and the band diagram shown in inset. All curves are offset for clarity.

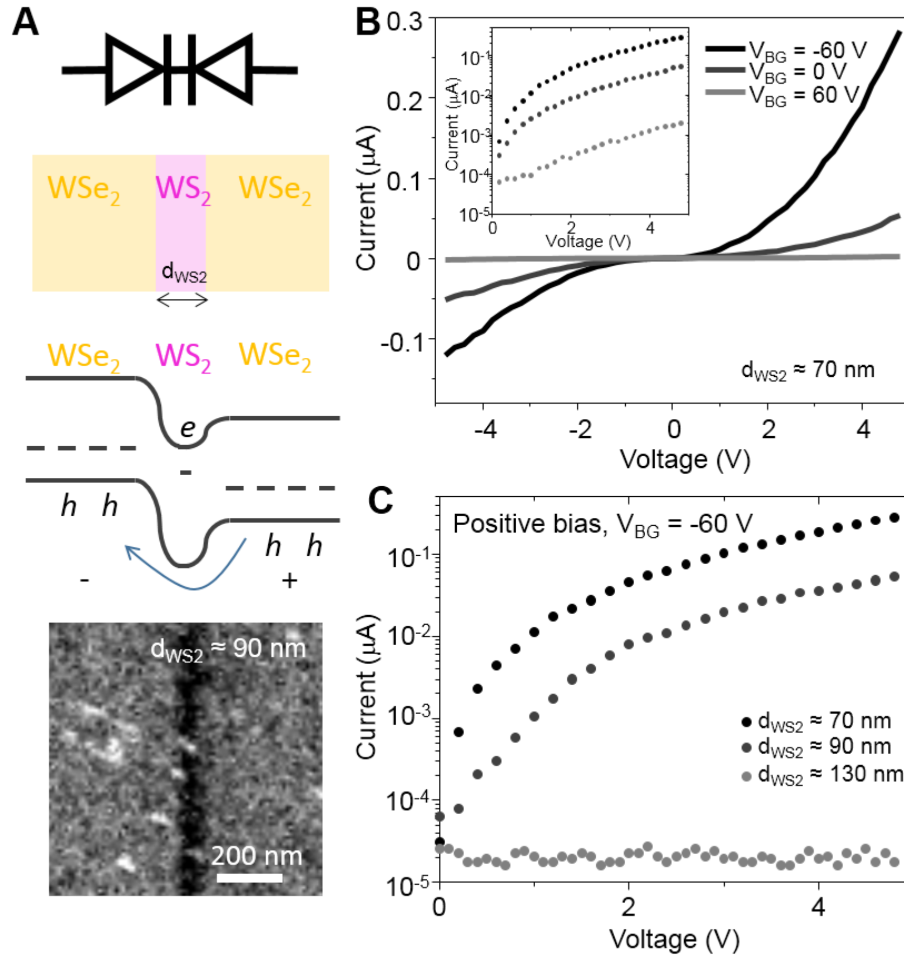

Fig. S9. Electrical transport of $WSe_2/WS_2/WSe_2$ double heterostructure transistors. (**A**) From top to bottom: symbol, schematic, band diagram of WSe_2-WS_2-WSe_2 double heterostructure (DH), and an SEM image of a representative DH device with $d_{WS2} \approx 90$ nm. (**B**) *I*-*V* curves for a DH device with $d_{WS2} \approx 70$ nm under different V_{BG}. (**C**) *I*-*V* curves for three DH devices with $d_{WS2} \approx 70$, 90, and 130 nm, respectively.

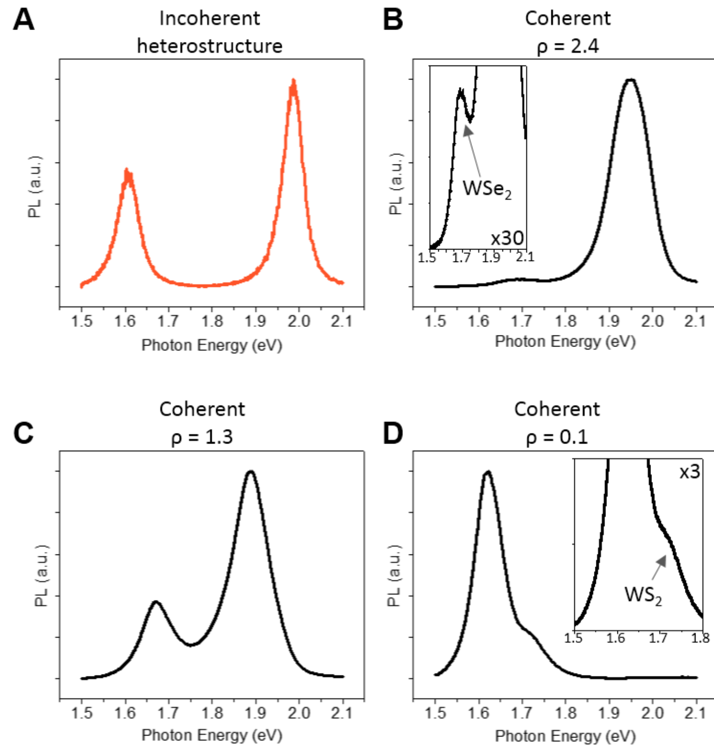

Fig. S10. PL spectra of WS_2/WSe_2 heterostructures. PL spectra of an incoherent WS_2/WSe_2 heterostructure (**A**) and three coherent WS_2/WSe_2 superlattices with ρ = 2.4 (**B**), 1.3 (**C**) and 0.1 (**D**). Insets show enlarged spectra for clarity.

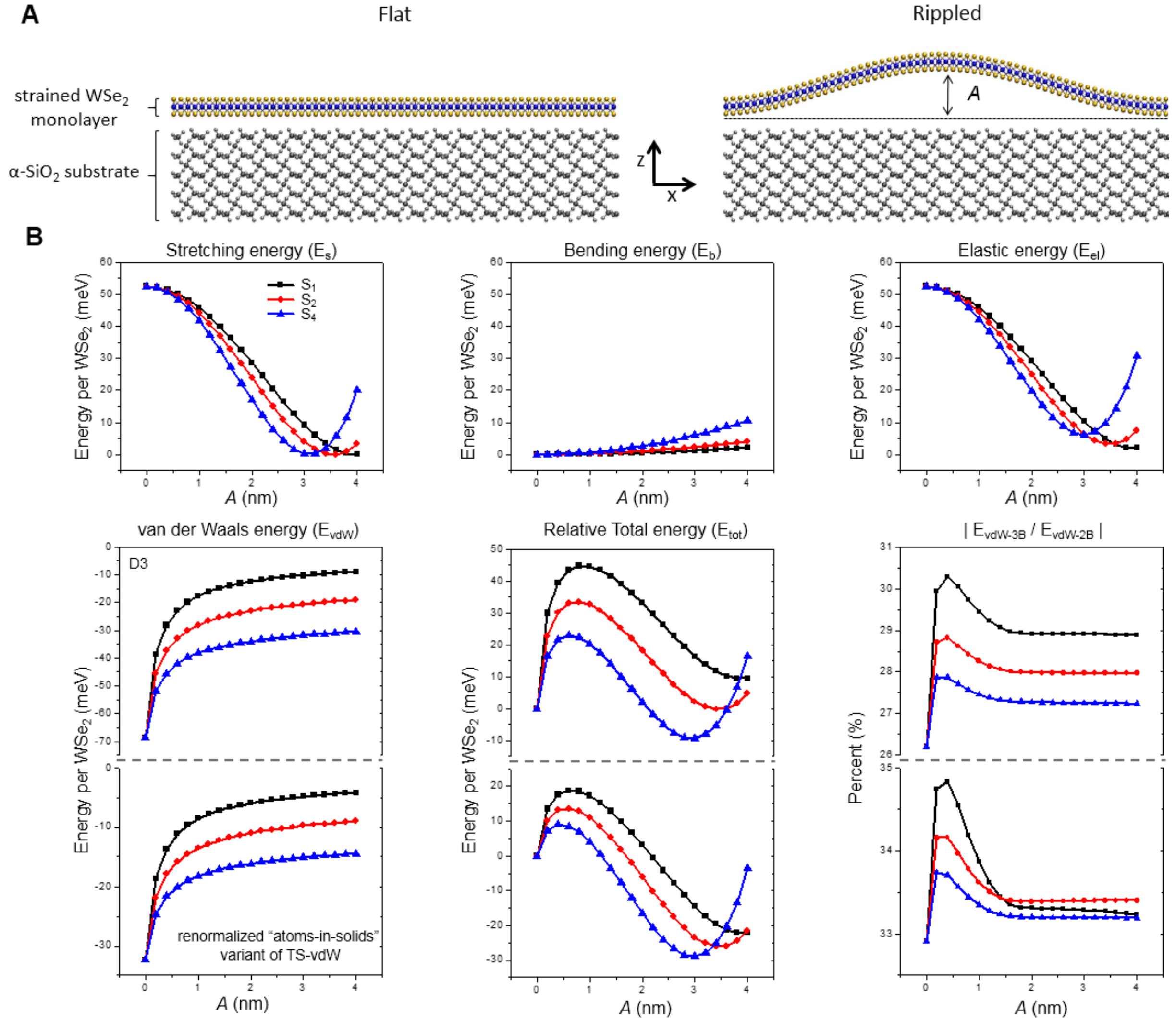

Fig. S11. Energetics of rippled WSe_2. (**A**) Schematic of the model for the flat-rippled configuration space in a strained WSe_2 monolayer grown on a SiO_2 substrate. (**B**) Stretching energy (E_s, upper left), bending energy (E_b, upper middle), elastic energy ($E_{el} = E_s + E_b$, upper right), interlayer van der Waals binding energy (E_{vdW}, lower left), and relative total energy ($E_{tot} = E_{el} + E_{vdW}$, lower middle) per WSe_2 as a function of the ripple height (A) for WSe_2 ripple shapes generated using the sinusoidal S_1, S_2, and S_4 transformations (see supplementary text for details). Lower right panel: ratio of three- to two-body interlayer vdW binding energy contributions, $|E_{vdW\text{-}3B}/E_{vdW\text{-}2B}|$, as a function of A for the various ripple shapes. Results for both vdW methods are presented here (see supplementary text for details).

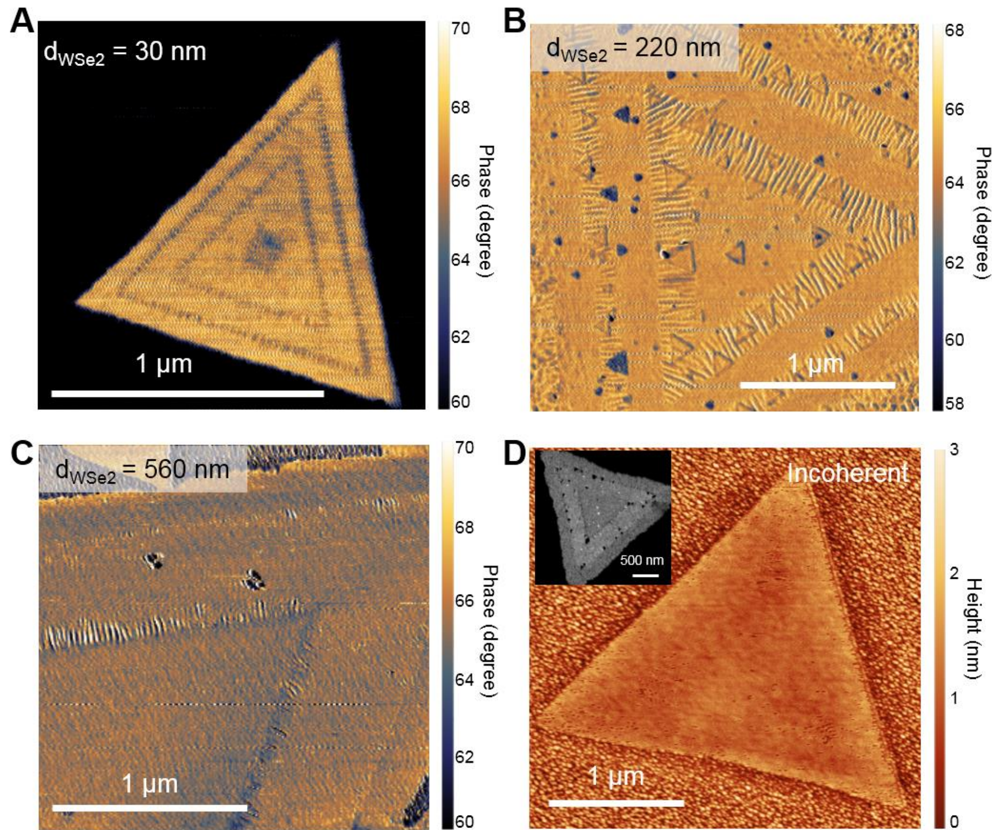

Fig. S12. AFM images of WS_2/WSe_2 heterostructures. (**A**-**C**) AFM phase images of WS_2/WSe_2 heterostructures with different d_{WSe2} of 30, 220, and 560 nm, respectively. Ripples are not continuous across the entire WSe_2 region in the superlattice with d_{WSe2} of 560 nm. (**D**) AFM height image of an incoherent WS_2/WSe_2 heterostructures showing no out-of-plane ripples. Inset: DF-TEM image of a similar sample showing the $WS_2/WSe_2/WS_2$ composition.

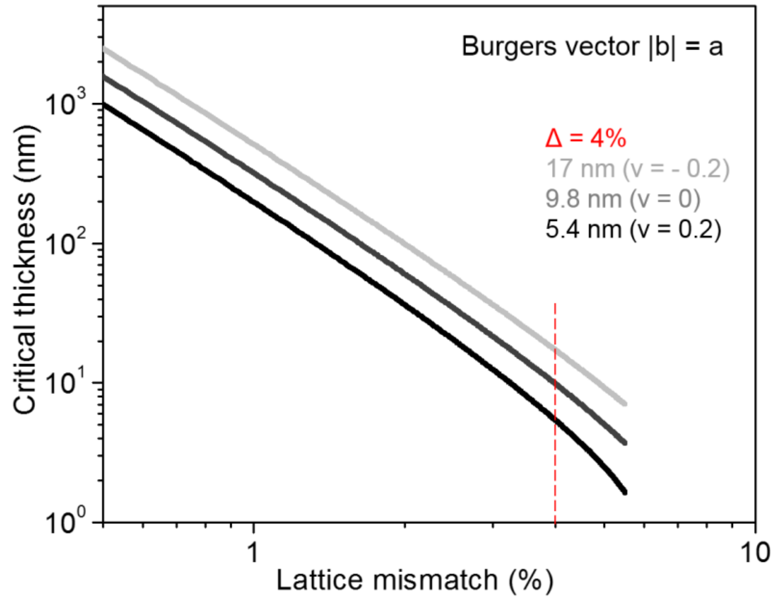

Fig. S13. Critical thickness. Critical thickness as a function of lattice mismatches, for ν = -0.2 (light gray), 0 (gray), and 0.2 (black), based on the People-Bean model. A critical thickness of 17 nm (ν = -0.2), 9.8 nm (ν = 0), and 5.4 nm (ν = 0.2) is estimated for the WS_2/WSe_2 epitaxial system with lattice mismatch of 4%.

Table S1. Supercell dimensions and growth time for different WS_2/WSe_2 superlattices.

Superlattice sample	$\{t_{WS2},t_{WSe2}\}$ /{min, min}	$\{d_{WS2},d_{WSe2}\}$ /{nm, nm}	t_{WS2}/t_{WSe2}	d_{WS2}/d_{WSe2}
Fig. 1C, left	{4, 3)	{110, 40}	1.33	2.75
Fig. 1C, right	{0.75, 7}	{30, 80}	0.11	0.38
Fig. 2F	{2, 5.5}	{75, 60}	0.36	1.25
Fig. 3B-I	{4, 3.5}	{120, 50}	1.14	2.40
Fig. 3B-II	{1.5, 4}	{100, 80}	0.38	1.25
Fig. 3B-III	{1, 4}	{70, 90}	0.25	0.78
Fig. 3B-IV	{1, 7}	{50, 100}	0.14	0.50
Fig. 3B-V	{0.83, 40}	{60, 600}	0.02	0.10

References

1. J. Wang, J. B. Neaton, H. Zheng, V. Nagarajan, S. B. Ogale, B. Liu, D. Viehland, V. Vaithyanathan, D. G. Schlom, U. V. Waghmare, N. A. Spaldin, K. M. Rabe, M. Wuttig, R. Ramesh, Epitaxial $BiFeO_3$ multiferroic thin film heterostructures. *Science* **299**, 1719–1722 (2003). doi:10.1126/science.1080615 Medline

2. D. G. Schlom, L.-Q. Chen, C. J. Fennie, V. Gopalan, D. A. Muller, X. Pan, R. Ramesh, R. Uecker, Elastic strain engineering of ferroic oxides. *MRS Bull.* **39**, 118–130 (2014). doi:10.1557/mrs.2014.1

3. J. Faist, F. Capasso, D. L. Sivco, C. Sirtori, A. L. Hutchinson, A. Y. Cho, Quantum cascade laser. *Science* **264**, 553–556 (1994). doi:10.1126/science.264.5158.553 Medline

4. S. Nakamura, The roles of structural imperfections in InGaN-based blue light-emitting diodes and laser diodes. *Science* **281**, 955–961 (1998). doi:10.1126/science.281.5379.956 Medline

5. A. K. Geim, I. V. Grigorieva, Van der Waals heterostructures. *Nature* **499**, 419–425 (2013). doi:10.1038/nature12385 Medline

6. D. Jariwala, T. J. Marks, M. C. Hersam, Mixed-dimensional van der Waals heterostructures. *Nat. Mater.* **16**, 170–181 (2017). doi:10.1038/nmat4703 Medline

7. D. Sarkar, X. Xie, W. Liu, W. Cao, J. Kang, Y. Gong, S. Kraemer, P. M. Ajayan, K. Banerjee, A subthermionic tunnel field-effect transistor with an atomically thin channel. *Nature* **526**, 91–95 (2015). doi:10.1038/nature15387 Medline

8. Q. H. Wang, K. Kalantar-Zadeh, A. Kis, J. N. Coleman, M. S. Strano, Electronics and optoelectronics of two-dimensional transition metal dichalcogenides. *Nat. Nanotechnol.* **7**, 699–712 (2012). doi:10.1038/nnano.2012.193 Medline

9. X. Xu, W. Yao, D. Xiao, T. F. Heinz, Spin and pseudospins in layered transition metal dichalcogenides. *Nat. Phys.* **10**, 343–350 (2014). doi:10.1038/nphys2942

10. W. Wu, L. Wang, Y. Li, F. Zhang, L. Lin, S. Niu, D. Chenet, X. Zhang, Y. Hao, T. F. Heinz, J. Hone, Z. L. Wang, Piezoelectricity of single-atomic-layer MoS_2 for energy conversion and piezotronics. *Nature* **514**, 470–474 (2014). doi:10.1038/nature13792 Medline

11. H. Zhu, Y. Wang, J. Xiao, M. Liu, S. Xiong, Z. J. Wong, Z. Ye, Y. Ye, X. Yin, X. Zhang, Observation of piezoelectricity in free-standing monolayer MoS_2. *Nat. Nanotechnol.* **10**, 151–155 (2015). doi:10.1038/nnano.2014.309 Medline

12. K. F. Mak, J. Shan, Photonics and optoelectronics of 2D semiconductor transition metal dichalcogenides. *Nat. Photonics* **10**, 216–226 (2016). doi:10.1038/nphoton.2015.282

13. X. Duan, C. Wang, J. C. Shaw, R. Cheng, Y. Chen, H. Li, X. Wu, Y. Tang, Q. Zhang, A. Pan, J. Jiang, R. Yu, Y. Huang, X. Duan, Lateral epitaxial growth of two-dimensional layered semiconductor heterojunctions. *Nat. Nanotechnol.* **9**, 1024–1030 (2014). doi:10.1038/nnano.2014.222 Medline

14. Y. Gong, J. Lin, X. Wang, G. Shi, S. Lei, Z. Lin, X. Zou, G. Ye, R. Vajtai, B. I. Yakobson, H. Terrones, M. Terrones, B. K. Tay, J. Lou, S. T. Pantelides, Z. Liu, W. Zhou, P. M.

Ajayan, Vertical and in-plane heterostructures from WS_2/MoS_2 monolayers. *Nat. Mater.* **13**, 1135–1142 (2014). doi:10.1038/nmat4091 Medline

15. C. Huang, S. Wu, A. M. Sanchez, J. J. P. Peters, R. Beanland, J. S. Ross, P. Rivera, W. Yao, D. H. Cobden, X. Xu, Lateral heterojunctions within monolayer $MoSe_2$-WSe_2 semiconductors. *Nat. Mater.* **13**, 1096–1101 (2014). doi:10.1038/nmat4064 Medline
16. M.-Y. Li, Y. Shi, C.-C. Cheng, L.-S. Lu, Y.-C. Lin, H.-L. Tang, M.-L. Tsai, C.-W. Chu, K.-H. Wei, J.-H. He, W.-H. Chang, K. Suenaga, L.-J. Li, Epitaxial growth of a monolayer WSe2-MoS2 lateral p-n junction with an atomically sharp interface. *Science* **349**, 524–528 (2015). doi:10.1126/science.aab4097 Medline
17. K. Chen, X. Wan, J. Wen, W. Xie, Z. Kang, X. Zeng, H. Chen, J.-B. Xu, Electronic properties of MoS_2-WS_2 heterostructures synthesized with two-step lateral epitaxial strategy. *ACS Nano* **9**, 9868–9876 (2015). doi:10.1021/acsnano.5b03188 Medline
18. Y. Gong, S. Lei, G. Ye, B. Li, Y. He, K. Keyshar, X. Zhang, Q. Wang, J. Lou, Z. Liu, R. Vajtai, W. Zhou, P. M. Ajayan, Two-step growth of two-dimensional $WSe_2/MoSe_2$ heterostructures. *Nano Lett.* **15**, 6135–6141 (2015). doi:10.1021/acs.nanolett.5b02423 Medline
19. X. Q. Zhang, C. H. Lin, Y. W. Tseng, K. H. Huang, Y. H. Lee, Synthesis of lateral heterostructures of semiconducting atomic layers. *Nano Lett.* **15**, 410–415 (2015). doi:10.1021/nl503744f Medline
20. H. Heo, J. H. Sung, G. Jin, J.-H. Ahn, K. Kim, M.-J. Lee, S. Cha, H. Choi, M.-H. Jo, Rotation-misfit-free heteroepitaxial stacking and stitching growth of hexagonal transition-metal dichalcogenide monolayers by nucleation kinetics controls. *Adv. Mater.* **27**, 3803–3810 (2015). doi:10.1002/adma.201500846 Medline
21. K. Bogaert, S. Liu, J. Chesin, D. Titow, S. Gradečak, S. Garaj, Diffusion-mediated synthesis of MoS_2/WS_2 lateral heterostructures. *Nano Lett.* **16**, 5129–5134 (2016). doi:10.1021/acs.nanolett.6b02057 Medline
22. K. Kang, S. Xie, L. Huang, Y. Han, P. Y. Huang, K. F. Mak, C.-J. Kim, D. Muller, J. Park, High-mobility three-atom-thick semiconducting films with wafer-scale homogeneity. *Nature* **520**, 656–660 (2015). doi:10.1038/nature14417 Medline
23. S. Helveg, J. V. Lauritsen, E. Laegsgaard, I. Stensgaard, J. K. Nørskov, B. S. Clausen, H. Topsøe, F. Besenbacher, Atomic-scale structure of single-layer MoS_2 nanoclusters. *Phys. Rev. Lett.* **84**, 951–954 (2000). doi:10.1103/PhysRevLett.84.951 Medline
24. J. V. Lauritsen, J. Kibsgaard, S. Helveg, H. Topsøe, B. S. Clausen, E. Laegsgaard, F. Besenbacher, Size-dependent structure of MoS_2 nanocrystals. *Nat. Nanotechnol.* **2**, 53–58 (2007). doi:10.1038/nnano.2006.171 Medline
25. M. W. Tate, P. Purohit, D. Chamberlain, K. X. Nguyen, R. Hovden, C. S. Chang, P. Deb, E. Turgut, J. T. Heron, D. G. Schlom, D. C. Ralph, G. D. Fuchs, K. S. Shanks, H. T. Philipp, D. A. Muller, S. M. Gruner, High dynamic range pixel array detector for scanning transmission electron microscopy. *Microsc. Microanal.* **22**, 237–249 (2016). doi:10.1017/S1431927615015664 Medline

26. P. Johari, V. B. Shenoy, Tuning the electronic properties of semiconducting transition metal dichalcogenides by applying mechanical strains. *ACS Nano* **6**, 5449–5456 (2012). doi:10.1021/nn301320r Medline

27. Y. Wang, C. Cong, W. Yang, J. Shang, N. Peimyoo, Y. Chen, J. Kang, J. Wang, W. Huang, T. Yu, Strain-induced direct–indirect bandgap transition and phonon modulation in monolayer WS_2. *Nano Res.* **8**, 2562–2572 (2015). doi:10.1007/s12274-015-0762-6

28. R. Schmidt *et al.*, Reversible uniaxial strain tuning in atomically thin WSe2. *2D Mater.* **3**, 021011 (2016).

29. R. Frisenda, M. Drüppel, R. Schmidt, S. Michaelis de Vasconcellos, D. Perez de Lara, R. Bratschitsch, M. Rohlfing, A. Castellanos-Gomez, Biaxial strain tuning of the optical properties of single-layer transition metal dichalcogenides. *npj 2D Mater. Appl.* **1**, 10 (2017). doi:10.1038/s41699-017-0013-7

30. Y. Klein, E. Efrati, E. Sharon, Shaping of elastic sheets by prescription of non-Euclidean metrics. *Science* **315**, 1116–1120 (2007). doi:10.1126/science.1135994 Medline

31. B. Davidovitch, R. D. Schroll, D. Vella, M. Adda-Bedia, E. A. Cerda, Prototypical model for tensional wrinkling in thin sheets. *Proc. Natl. Acad. Sci. U.S.A.* **108**, 18227–18232 (2011). doi:10.1073/pnas.1108553108 Medline

32. D. Nandwana, E. Ertekin, Ripples, strain, and misfit dislocations: Structure of graphene-boron nitride superlattice interfaces. *Nano Lett.* **15**, 1468–1475 (2015). doi:10.1021/nl505005t Medline

33. A. Ambrosetti, N. Ferri, R. A. DiStasio Jr., A. Tkatchenko, Wavelike charge density fluctuations and van der Waals interactions at the nanoscale. *Science* **351**, 1171–1176 (2016). doi:10.1126/science.aae0509 Medline

34. J. W. Matthews, A. E. Blakeslee, Defects in epitaxial multilayers: I. Misfit dislocations. *J. Cryst. Growth* **27**, 118–125 (1974).

35. R. People, J. C. Bean, Calculation of critical layer thickness versus lattice mismatch for Ge_xSi_{1-x}/Si strained-layer heterostructures. *Appl. Phys. Lett.* **47**, 322–324 (1985). doi:10.1063/1.96206

36. S. Najmaei, Z. Liu, W. Zhou, X. Zou, G. Shi, S. Lei, B. I. Yakobson, J.-C. Idrobo, P. M. Ajayan, J. Lou, Vapour phase growth and grain boundary structure of molybdenum disulphide atomic layers. *Nat. Mater.* **12**, 754–759 (2013). doi:10.1038/nmat3673 Medline

37. D. Dumcenco, D. Ovchinnikov, K. Marinov, P. Lazić, M. Gibertini, N. Marzari, O. Lopez Sanchez, Y.-C. Kung, D. Krasnozhon, M.-W. Chen, S. Bertolazzi, P. Gillet, A. Fontcuberta i Morral, A. Radenovic, A. Kis, Large-area epitaxial monolayer MoS_2. *ACS Nano* **9**, 4611–4620 (2015). doi:10.1021/acsnano.5b01281 Medline

38. D. Ruzmetov, K. Zhang, G. Stan, B. Kalanyan, G. R. Bhimanapati, S. M. Eichfeld, R. A. Burke, P. B. Shah, T. P. O’Regan, F. J. Crowne, A. G. Birdwell, J. A. Robinson, A. V. Davydov, T. G. Ivanov, Vertical 2D/3D semiconductor heterostructures based on epitaxial molybdenum disulfide and gallium nitride. *ACS Nano* **10**, 3580–3588 (2016). doi:10.1021/acsnano.5b08008 Medline

39. A. M. van der Zande, P. Y. Huang, D. A. Chenet, T. C. Berkelbach, Y. You, G.-H. Lee, T. F. Heinz, D. R. Reichman, D. A. Muller, J. C. Hone, Grains and grain boundaries in highly crystalline monolayer molybdenum disulphide. *Nat. Mater.* **12**, 554–561 (2013). doi:10.1038/nmat3633 Medline

40. D. A. Muller, Y. Han, K. X. Nguyen, M. W. Tate, P. Purohit, S. Xie, J. Park, S. M. Gruner, Electron diffraction from a single atom and optimal signal detection. *Microsc. Microanal.* **22** (S3), 846–847 (2016). doi:10.1017/S1431927616005079

41. R. W. Havener, S.-Y. Ju, L. Brown, Z. Wang, M. Wojcik, C. S. Ruiz-Vargas, J. Park, High-throughput graphene imaging on arbitrary substrates with widefield Raman spectroscopy. *ACS Nano* **6**, 373–380 (2012). doi:10.1021/nn2037169 Medline

42. D. Cakir, F. M. Peeters, C. Sevik, Mechanical and thermal properties of h-MX_2 (M=Cr, Mo, W; X=O, S, Se, Te) monolayers: A comparative study. *Appl. Phys. Lett.* **104**, 203110 (2014). doi:10.1063/1.4879543

43. J. Kang, S. Tongay, J. Zhou, J. Li, J. Wu, Band offsets and heterostructures of two-dimensional semiconductors. *Appl. Phys. Lett.* **102**, 012111 (2013). doi:10.1063/1.4774090

44. Atomistic ToolKit version 2014.3, QuantumWise A/S (www.quantumwise.com).

45. C. Lee, X. Wei, J. W. Kysar, J. Hone, Measurement of the elastic properties and intrinsic strength of monolayer graphene. *Science* **321**, 385–388 (2008). doi:10.1126/science.1157996 Medline

46. K. Liu, Q. Yan, M. Chen, W. Fan, Y. Sun, J. Suh, D. Fu, S. Lee, J. Zhou, S. Tongay, J. Ji, J. B. Neaton, J. Wu, Elastic properties of chemical-vapor-deposited monolayer MoS_2, WS_2, and their bilayer heterostructures. *Nano Lett.* **14**, 5097–5103 (2014). doi:10.1021/nl501793a Medline

47. D. Vella, J. Bico, A. Boudaoud, B. Roman, P. M. Reis, The macroscopic delamination of thin films from elastic substrates. *Proc. Natl. Acad. Sci. U.S.A.* **106**, 10901–10906 (2009). doi:10.1073/pnas.0902160106 Medline

48. J. W. Jiang, The buckling of single-layer MoS_2 under uniaxial compression. *Nanotechnology* **25**, 355402 (2014). doi:10.1088/0957-4484/25/35/355402 Medline

49. Y. Huang, J. Wu, K. C. Hwang, Thickness of graphene and single-wall carbon nanotubes. *Phys. Rev. B* **74**, 245413 (2006). doi:10.1103/PhysRevB.74.245413

50. J.-W. Jiang, Z. Qi, H. S. Park, T. Rabczuk, Elastic bending modulus of single-layer molybdenum disulfide (MoS_2): Finite thickness effect. *Nanotechnology* **24**, 435705 (2013). doi:10.1088/0957-4484/24/43/435705 Medline

51. D. Akinwande, C. J. Brennan, J. S. Bunch, P. Egberts, J. R. Felts, H. Gao, R. Huang, J.-S. Kim, T. Li, Y. Li, K. M. Liechti, N. Lu, H. S. Park, E. J. Reed, P. Wang, B. I. Yakobson, T. Zhang, Y.-W. Zhang, Y. Zhou, Y. Zhu, A review on mechanics and mechanical properties of 2D materials: Graphene and beyond. *Extrem. Mech. Lett.* **13**, 42–77 (2017). doi:10.1016/j.eml.2017.01.008

52. J. Zhao, Q. Deng, T. H. Ly, G. H. Han, G. Sandeep, M. H. Rümmeli, Two-dimensional membrane as elastic shell with proof on the folds revealed by three-dimensional atomic mapping. *Nat. Commun.* **6**, 8935 (2015). doi:10.1038/ncomms9935 Medline

53. S. Grimme, J. Antony, S. Ehrlich, H. Krieg, A consistent and accurate ab initio parametrization of density functional dispersion correction (DFT-D) for the 94 elements H-Pu. *J. Chem. Phys.* **132**, 154104 (2010). doi:10.1063/1.3382344 Medline

54. S. Grimme, S. Ehrlich, L. Goerigk, Effect of the damping function in dispersion corrected density functional theory. *J. Comput. Chem.* **32**, 1456–1465 (2011). doi:10.1002/jcc.21759 Medline

55. D. G. A. Smith, L. A. Burns, K. Patkowski, C. D. Sherrill, Revised damping parameters for the D3 dispersion correction to density functional theory. *J. Phys. Chem. Lett.* **7**, 2197–2203 (2016). doi:10.1021/acs.jpclett.6b00780 Medline

56. G.-X. Zhang, A. Tkatchenko, J. Paier, H. Appel, M. Scheffler, Van der Waals interactions in ionic and semiconductor solids. *Phys. Rev. Lett.* **107**, 245501 (2011). doi:10.1103/PhysRevLett.107.245501 Medline

57. V. G. Ruiz, W. Liu, E. Zojer, M. Scheffler, A. Tkatchenko, Density-functional theory with screened van der Waals interactions for the modeling of hybrid inorganic-organic systems. *Phys. Rev. Lett.* **108**, 146103 (2012). doi:10.1103/PhysRevLett.108.146103 Medline

58. A. Tkatchenko, M. Scheffler, Accurate molecular van der Waals interactions from ground-state electron density and free-atom reference data. *Phys. Rev. Lett.* **102**, 073005 (2009). doi:10.1103/PhysRevLett.102.073005 Medline

59. O. A. von Lilienfeld, A. Tkatchenko, Two- and three-body interatomic dispersion energy contributions to binding in molecules and solids. *J. Chem. Phys.* **132**, 234109 (2010). doi:10.1063/1.3432765 Medline

60. Q. Ouyang, S. Zeng, L. Jiang, L. Hong, G. Xu, X.-Q. Dinh, J. Qian, S. He, J. Qu, P. Coquet, K.-T. Yong, Sensitivity enhancement of transition metal dichalcogenides/silicon nanostructure-based surface plasmon resonance biosensor. *Sci. Rep.* **6**, 28190 (2016). doi:10.1038/srep28190 Medline

61. J. E. Ayers, Mismatched Heteroepitaxial Growth and Strain Relaxation, in *Heteroepitaxy of Semiconductors: Theory, Growth, and Characterization* (CRC Press, 2007), pp. 161–248.